Effect of solution heat treatment on the microstructure and crystallographic texture of IN939 fabricated by powder bed fusion-laser beam

Merve Nur Doğu [a,b,c,*,1], *Seren Ozer* [d,e,**,1], *Mustafa Alp Yalçın* [f], *Kemal Davut* [g], *Güney Mert Bilgin* [e], *Muhannad Ahmed Obeidi* [a,b,c], *Håkan Brodin* [h], *Hengfeng Gu* [i], *Dermot Brabazon* [a,b,c]

[a] *I-Form Advanced Manufacturing Research Centre, Dublin City University, Dublin, Ireland*
[b] *Advanced Processing Technology Research Centre, Dublin City University, Dublin, Ireland*
[c] *School of Mechanical & Manufacturing Engineering, Dublin City University, Dublin, Ireland*
[d] *Department of Metallurgical and Materials Engineering, Atılım University, Ankara, Turkey*
[e] *Department of Metallurgical and Materials Engineering, Middle East Technical University, Ankara, Turkey*
[f] *Metal Forming Center of Excellence, Atılım University, Ankara, Turkey*
[g] *Department of Materials Science and Engineering, Izmir Institute of Technology, Izmir, Turkey*
[h] *Siemens Energy AB, Slottsvägen 2-6, 612 83 Finspång, Sweden*
[i] *Ansys Inc., 1441 W Ute Blvd, Suite 335, Park City, UT 84098, USA*

ARTICLE INFO

ABSTRACT

The effect of various solution heat treatment temperatures (i.e., 1120, 1160, 1200 and 1240 °C) on the microstructure, grain morphology and crystallographic texture of IN939 fabricated by powder bed fusion-laser beam (PBF-LB) was investigated. Microstructural analyses showed that the high-temperature gradient and rapid solidification of the PBF-LB processing caused different resulting microstructures compared to conventionally produced counterparts. The melt pool morphologies and laser scanning paths were examined in the as-fabricated samples in the XZ- and XY-planes, respectively. After the application of solution heat treatment at 1120 °C, the as-fabricated PBF-LB initial microstructure was still apparent. For solution heat treatments of 1200 °C and above, the melt pool and scanning path morphologies disappeared and converted into a mixture of columnar grains in the XZ-plane and equiaxed grains in the XY-plane. On the other hand, large equiaxed grains were observed when the samples were solutionized at 1240 °C. Additionally, γ′ phase precipitated within the matrix after all solution heat treatment conditions, which led to increase in the microhardness values. According to electron backscatter diffraction (EBSD) analyses, both as-fabricated and solution heat-treated samples had intense texture with {001} plane normal parallel to the building direction. The first recrystallized grains began to appear when the samples were subjected to the solution heat treatment at 1160 °C and the fraction of the recrystallized grains increased with increasing temperature, as

---

* Corresponding author.
** Corresponding author.
E-mail addresses: mervenur.dogu@dcu.ie (M.N. Doğu), ozer.seren@metu.edu.tr (S. Ozer).
[1] The authors have made an equal contribution to the article.

supported by kernel average misorientation (KAM) and grain spread orientation (GOS) analyses.

1. Introduction

The production of aerospace components, which are mainly made from nickel-based superalloys, is often challenged by conventional manufacturing methods due to their intricate geometries, e.g., cooling channels in the turbine blade. Some undesired microstructural features including macro-segregation of alloying elements and uncontrolled grain growth may develop in the cast material due to the slow cooling rate [1,2]. In recent years, an alternative method called powder bed fusion-laser beam (PBF-LB), which is one of the well-known metal additive manufacturing (AM) techniques, has received significant attention in various industries to produce components. The PBF-LB method utilizes a focused laser beam to melt the powders layer-by-layer based on a 3D computer-aided-design (CAD) model data [3]. This method provides an improvement in product quality by enabling the production of functional metallic components with complex geometries in a single step that eliminates assembly operations [4]. In contrast to the conventional manufacturing methods, it offers a wide range of advantages in terms of design freedom, net-near-shaping capability, increasing component life-time as well as reduction of material waste and tooling cost [5,6]. However, the high-temperature gradient and rapid solidification rate of the PBF-LB method may cause some process-induced defects in the microstructure of produced components. These defects can be described as the formation of topologically close-packed (TCP) phases, directional grain growth, segregation of elements, high residual stresses, formation of porosities and lack of fusion (LOF) and micro-cracks [7,8]. These micro-cracks can be divided into liquation/solidification cracks due to the formation of low melting phases on the grain boundaries and strain-age cracks due to residual stress from the gamma-prime phase development [9].

The effect of process parameters and post-processing heat treatments on the mechanical performance of nickel-based superalloys such as IN718 fabricated by the PBF-LB has recently been investigated [10]. However, its applications are limited to operating temperatures up to ~650 °C because of the coarsening of the grains [1] and the transformation of the strengthening γ'' (Ni$_3$Nb) phase into the stable and brittle δ phase at higher temperatures, as reported in detail in our previous study [11]. On the other hand, Inconel 939 (IN939) is a promising candidate used for producing gas turbine engine components that require prolonged working periods at operating temperatures up to ~ 850 °C [1]. Nevertheless, there are only a few studies in the literature on the microstructure and mechanical properties of IN939 fabricated by additive manufacturing methods. IN939 is a precipitation-hardenable nickel-based superalloy, which is strengthened mainly by the formation of L12-ordered γ' (Ni$_3$(Al,Ti)) precipitates in the γ matrix [1,12]. Nowadays, gas turbine blades/vanes, fuel nozzles, casing and other structural components are produced using the cast form of this alloy due to its remarkable properties such as good creep resistance and high-temperature strength combined with excellent oxidation and corrosion resistance [2,13,14]. Kanagarajah et al. [14] investigated the effect of the standard heat treatment (solutionizing at 1160 °C for 4 h followed by aging at 850 °C for 16 h) on the microstructure and mechanical behavior of the IN939 produced by the PBF-LB. They reported that the as-produced samples showed higher tensile properties than the cast material owing to its finer microstructure. However, the results obtained from high-temperature mechanical tests revealed that the samples exhibited lower tensile properties than the cast ones, suggesting that solution heat treatment should be adapted for materials produced by PBF-LB. Another study conducted by Philpott et al. [15] mainly focused on the effect of various heat treatments on the microstructure of the IN939 produced by PBF-LB, particularly the precipitation of the strengthening γ' phase and carbides.

It should be noted that the microstructure and the resulting properties of the materials produced by the PBF-LB method are quite different from their conventional counterparts. Therefore, the standard heat treatment applied to conventionally produced IN939 may not sufficiently improve the properties of materials produced with the PBF-LB. The typical heat treatment procedure for IN939 includes solution heat treatment followed by aging. Solution heat treatment is usually carried out above the γ' solvus temperature to obtain a homogeneous distribution of alloying elements throughout the solid solution. In addition, the dissolution of TCP phases is another issue that is significant for the aging step, which is effective in improving the mechanical properties [12]. The above-mentioned findings from the literature reveal that a detailed study of the microstructure, grain morphology and crystallographic texture on the as-fabricated and solution heat-treated parts is still missing. Furthermore, there are limited studies on the recrystallization phenomena and grain growth kinetics of the IN939 produced by the PBF-LB method. This study aims at closing this gap by studying the influence of solution heat treatment carried out at four different temperatures (1120, 1160, 1200 and 1240 °C) on the microstructure, recrystallization and texture of IN939 samples fabricated by the PBF-LB.

2. Experimental procedure

2.1. Starting material

Gas-atomized IN939 powder (Truform 939-N65, Praxair Surface Technologies) was used as a starting material for the fabrication of the samples by the PBF-LB method. The chemical composition of the powder (as given in Table 1) delivered

Table 1 – Elemental composition of the starting gas-atomized IN939 powder.

Elements (wt.%)					
Al	Co	Cr	Nb	Ta	Ti
1.9	18.9	22.8	1.0	1.4	3.8
W	B	C	O	N	Ni
2.0	0.004	0.16	0.014	0.009	Bal.

by the material supplier was also verified by the energy dispersive spectroscopy (EDS) analysis, using scanning electron microscope (SEM) (ZEISS Merlin® FE-SEM, Germany).

As shown in Fig. 1(a and b), the powder is mostly spherical, containing a few satellite particles which may form due to the rapid solidification associated with the gas atomization process or the recycling of the PBF-LB precursor powder [16]. A Malvern Mastersizer 3000 with an Aero S dispersion unit was used to measure the particle size distribution which was in the range of 17.6 (D_{10}) to 52.4 (D_{90}) µm with an average particle size of 30.2 µm (D_{50}). The cross-section of the powder particle (Fig. 1(c)) revealed that the powder exhibited a dendritic microstructure including some small pores around 1–2 µm, especially near the surface of the particles. Additionally, the average grain size of the random-texturized particles was measured as 1.6 ± 0.4 µm, as can be seen in the inverse pole figure (IPF) map (Fig. 1(d)). It should be noted that the morphology and average particle size of the powder are important parameters to enable good powder fluidity and packing within the PBF-LB process, in order to obtain fully dense components and related good mechanical properties.

2.2. Fabrication of IN939 with the PBF-LB method

IN939 cubic samples ($10 \times 10 \times 10$ mm^3), as shown in Fig. 2, were fabricated under a protective argon atmosphere using Aconity MINI (GmbH) metal 3D printer equipped with a 200 W fiber laser manufactured by IPG Photonics with a wavelength of 1068 nm. Process parameters used for the fabrication of the samples are given in Table 2. During the processing, a supply factor of 3 was used to provide enough powder to build area for each layer. In addition, the volumetric energy density, VED (J/mm^3) was calculated as 104.2 J/mm^3 by taking the laser power, P (W), laser speed, υ (mm/s), layer thickness, t (mm) and hatch spacing, h (mm) into account using the following equation.

$$VED = \frac{P}{υ.t.h} \tag{1}$$

2.3. Solution heat treatment procedure

To investigate the effect of the underlying microstructure on the crystallographic texture, some of the as-fabricated samples were subjected to solution heat treatment at 1120, 1160, 1200 and 1240 °C for 4h, followed by air-cooling to room temperature. Those samples are named as "SHT" followed by the solutionizing temperature, e.g., SHT1120.
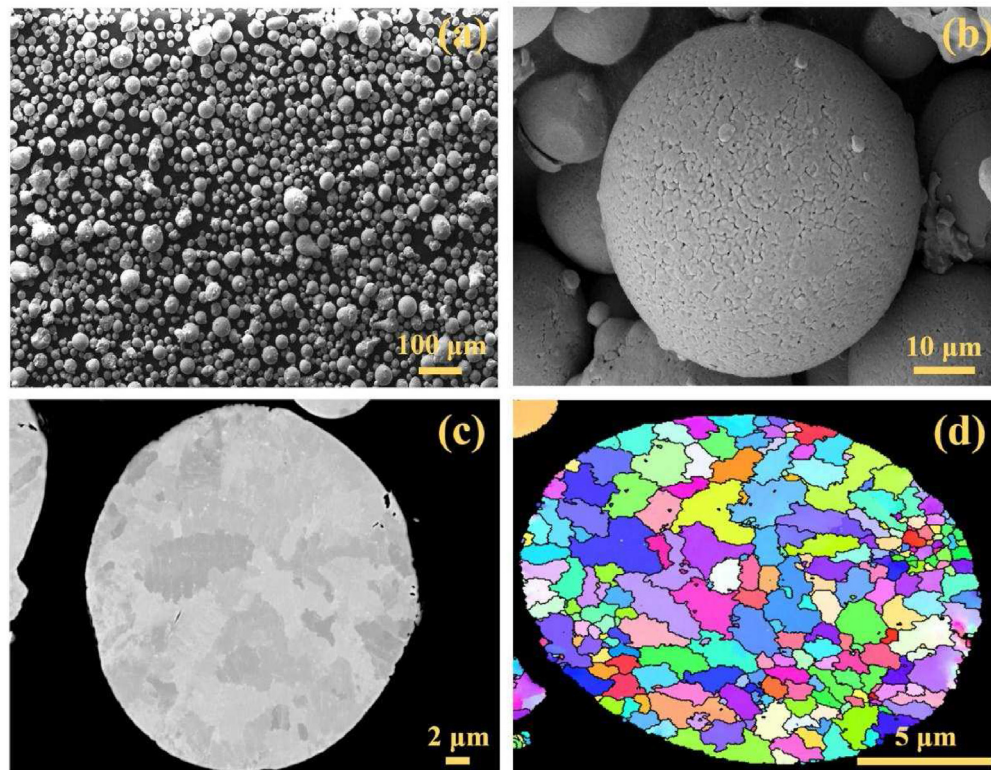
Fig. 1 – Gas-atomized IN939 powder utilized for the PBF-LB processing: (a, b) SEM images, (c) SEM-BSE image of a cross-section of a particle showing a dendritic microstructure and (d) the IPF map of the cross-section of a particle.
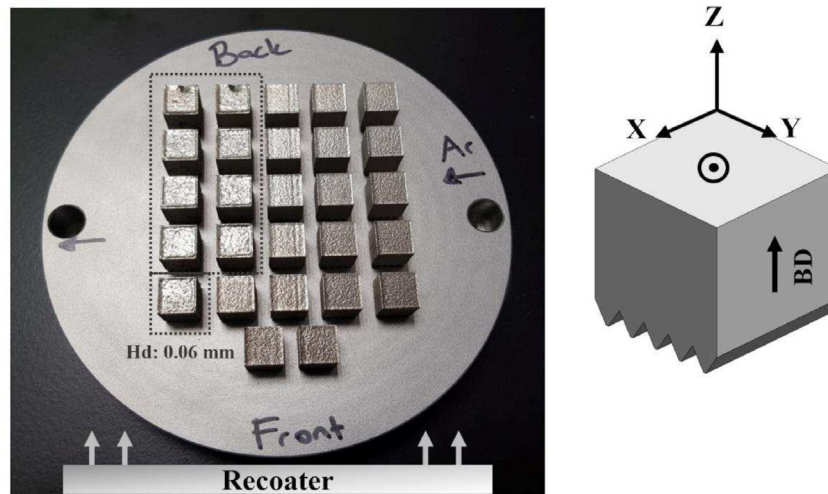
Fig. 2 – Picture of the PBF-LB built samples and schematics of the observation directions used for microstructural examinations (BD: build direction).

2.4. Microstructural characterization

Microstructural observations of the samples were carried out using both an optical microscope (Nikon Eclipse LV150) and SEM operated at 20 kV accelerating voltage. For the metallographic examination, IN939 cubic samples were sectioned by a precision abrasive cutter (Buehler IsoMet 5000) to investigate both observation directions, i.e., parallel to the building direction and perpendicular to the building direction, attributed to XZ-plane and XY-plane, respectively. Before the analyses, the surfaces of the samples were prepared using standard metallographic methods (i.e., ground with SiC emery papers up to 2500 grit size and polished with progressively finer diamond suspensions (first 6 μm and then 1 μm)), then cleaned with deionized water and ethanol, and subsequently etched using Glyceregia reagent (15 ml HCl, 10 ml glycerol and 5 ml HNO_3) for 50—60 s. In addition, at least five EDS analyses were performed to obtain the average atomic and/or weight percentages of the elements for accurately compositional analyses.

Electron backscatter diffraction (EBSD) technique was carried out to examine the microstructural details including grain structure, misorientation and crystallographic texture of both as-fabricated and solution heat-treated samples. Unlike the previous preparation methods, samples were polished with a colloidal silica suspension using the oxide polishing suspension (OP—S) (Struers Inc., Denmark) after grinding and polishing steps. For analyses, Zeiss Merlin field emission gun (FEG) scanning electron microscope (SEM) equipped with EDAX/TSL EBSD system and a Hikari EBSD camera were utilized with the accelerating voltage of 15 kV, beam current of

6.0 nA and the working distance of 14 mm; the mapping areas of 500 x 500 μm were indexed on a hexagonal grid with a step size of 1 μm. Raw EBSD data was processed using TSL-OIM Analysis v7.3.1 software. Additionally, texture analyses were performed using the generalized spherical harmonic series expansion method of Bunge [17]. The harmonic series were expanded to a rank (L) of 34, and a Gaussian smoothing with a half-width of 5° was used.

2.5. Microhardness tests

Vickers microhardness tests were performed on the polished surfaces of the as-fabricated and solution heat-treated samples using a Zwick/Roell Zhu microhardness tester 2.5 with a load of 1 kg (denoted as HV1) and loading time of 20 s. The microhardness measurements were taken from at least 10 different points on each observation plane (i.e., XZ- and XY-planes) to obtain the average values of each sample.

3. Results

3.1. Microstructural analyses of the as-fabricated and solution heat-treated IN939 samples

The relative density of the as-fabricated sample was measured to be ca. 99.4% by Archimedes' method using an analytical balance (Sartorius Entris II Essential BCE124I—1S) having accuracy and repeatability of ±0.1 mg according to ASTM B962-13 [18]. Fig. 3 exhibits gas pores and some LOF regions (seen as black colored defects) in the PBF-LB as-fabricated and solution heat-treated samples. These defects generally form in nickel-based superalloys during the PBF-LB processing due to some reasons that will be further explained in the discussion section. Additionally, the relative density after solution heat-treatment as measured to the same level as in the as-fabricated material condition.

Fig. 4 shows optical microscope and SEM images of the as-fabricated IN939 sample for both observation directions. An

Table 2 – PBF-LB process parameters utilized in the present study.				
Laser power	Laser scan speed	Layer thickness	Hatch spacing	Hatch rotation
200 W	800 mm/s	0.04 mm	0.06 mm	67°
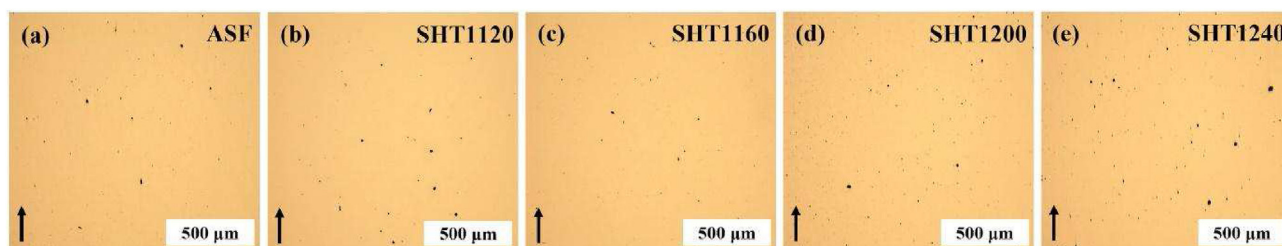
Fig. 3 — As-polished micrographs of the as-fabricated and solution heat-treated IN939 samples in the XZ-plane: (a) as-fabricated (ASF), (b) SHT1120, (c) SHT1160, (d) SHT1200 and (e) SHT1240 (the arrow represents the building direction).

arc-shaped melt pool morphology was observed in the XZ-plane (Fig. 4(a, c)) which was formed due to the Gaussian energy distribution of the laser beam which is applied during the PBF-LB process [19]. Whereas the laser beam scanning paths were observed in the XY-plane (Fig. 4(b, d)). Similar morphologies have been reported as typical characteristic microstructures found in additively manufactured parts in many studies [1,20]. It should be noted that the physical and mechanical properties of as-fabricated parts are highly dependent on the geometry of the melt pool morphology (i.e., shape, width and depth) influenced by the thermal history of the PBF-LB method. High magnification SEM image (Fig. 4(e)) showed that some cellular structures with sizes of ~0.5 μm and columnar dendrites with an average dendrite arm spacing of ~0.7 μm occurred within the structure.

Fig. 5 shows the optical images of the solution heat-treated samples in both observation directions. It can be seen in Fig. 5(a and b), the melt pool and scanning paths observed in the as-fabricated sample were still presented for the SHT1120 sample which means the solution temperature was insufficient to dissolve the initial microstructure. With increasing solution heat treatment temperature up to 1200 °C, the melt pool and scanning path morphologies disappeared and converted into a mixture of columnar grains in the XZ-plane and equiaxed grains in the XY-plane. On the other hand, large equiaxed grains were observed in the SHT1240 sample for both observation directions which indicates most of the grains started to grow after recrystallization. A more detailed examination of the microstructure results is given in the texture analysis section.

Further investigations revealed that many undissolved white particles with an average size of ~0.5 μm were observed in the grains, particularly along the grain boundaries, as given in Fig. 6(a–h). The low diffusion rate of the large elements makes the dissolution of this type of particles difficult as also stated by Komarasamy et al. [5]. Moreover, a large number of spherical-like nano-sized precipitates corresponding to γ′ phase homogeneously distributed in the matrix was observed, as can be seen in higher magnification SEM micrographs in Fig. 6(a1, c1, e1, g1). This observation is also in agreement with the study conducted by Shaikh AS [9]. According to the results obtained from Image J analyses, the size of γ′ phase was measured as 35 ± 12 nm, 56 ± 11 nm, 49 ± 9 nm and 40 ± 7 nm for the SHT1120, SHT1160, SHT1200 and SHT1240 samples, respectively. Additionally, plate-like phases were not observed during the SEM analyses. For this reason, it can be said that no significant η-phase was presented in the

microstructures as also reported in this study [9]. According to EDS analyses given in Fig. 7 and Table 3, some irregular-shaped MC type (rich in Ti, Nb and Ta) carbides were observed at the grain boundaries and also grain interior (Spot 1 and 2). Note that the accuracy of W detection in EDS analyses is limited due to the overlapping of W and Ta peaks and the minor alloying of this element in IN939.

3.2. Texture analysis of the as-fabricated and solution heat-treated IN939 samples

From PBF-LB processing, the grain structure and crystallographic texture vary along building and scanning directions, resulting in microstructure anisotropy. Detailed EBSD analyses were performed on the IN939 samples to investigate microstructure and texture. The grain structure of the samples can be clearly seen in the inverse pole figure (IPF) and image quality & grain boundaries (IQ & GBs) maps for both XZ- and XY-planes, as given in Figs. 8 and 9The as-fabricated sample showed a microstructure composed of columnar elongated grains along the build direction (in the XZ-plane). In contrast, equiaxed grains were present in the XY-plane. Additionally, the area-weighted average grain size of the as-fabricated sample was measured as 10.8 μm in the XZ-plane and 21.3 μm in the XY-plane. It has been reported that the rapid solidification of the melt pools during the PBF-LB processing causes the formation of finer microstructures compared to conventional manufacturing methods along with the improvement of mechanical performance of the alloys [21]. For the SHT1120, SHT1160 and SHT1200 samples, the elongated columnar grains in the XZ-plane and equiaxed grains in the XY-plane were still observed, similar to the as-fabricated one. Unlike the other samples, large equiaxed grains were observed in the SHT1240 sample for both observation directions. Thus, it can be revealed that the columnar grain structure was almost completely replaced by equiaxed grains when the sample was solutionized at 1240 °C. Furthermore, the average grain size of the samples increased with increasing solution heat treatment temperature, as can be seen in Fig. 11 and Table 4.

Pole figures (PFs) of the samples were obtained from the corresponding EBSD data to estimate the crystallographic orientations, as given in Fig. 10. Note that only the corresponding {001} PF and IPF with respect to building direction were represented for the texture analyses. As can be seen, the {001}//BD texture component was dominant, for both as-fabricated and solution heat-treated samples. The maximum
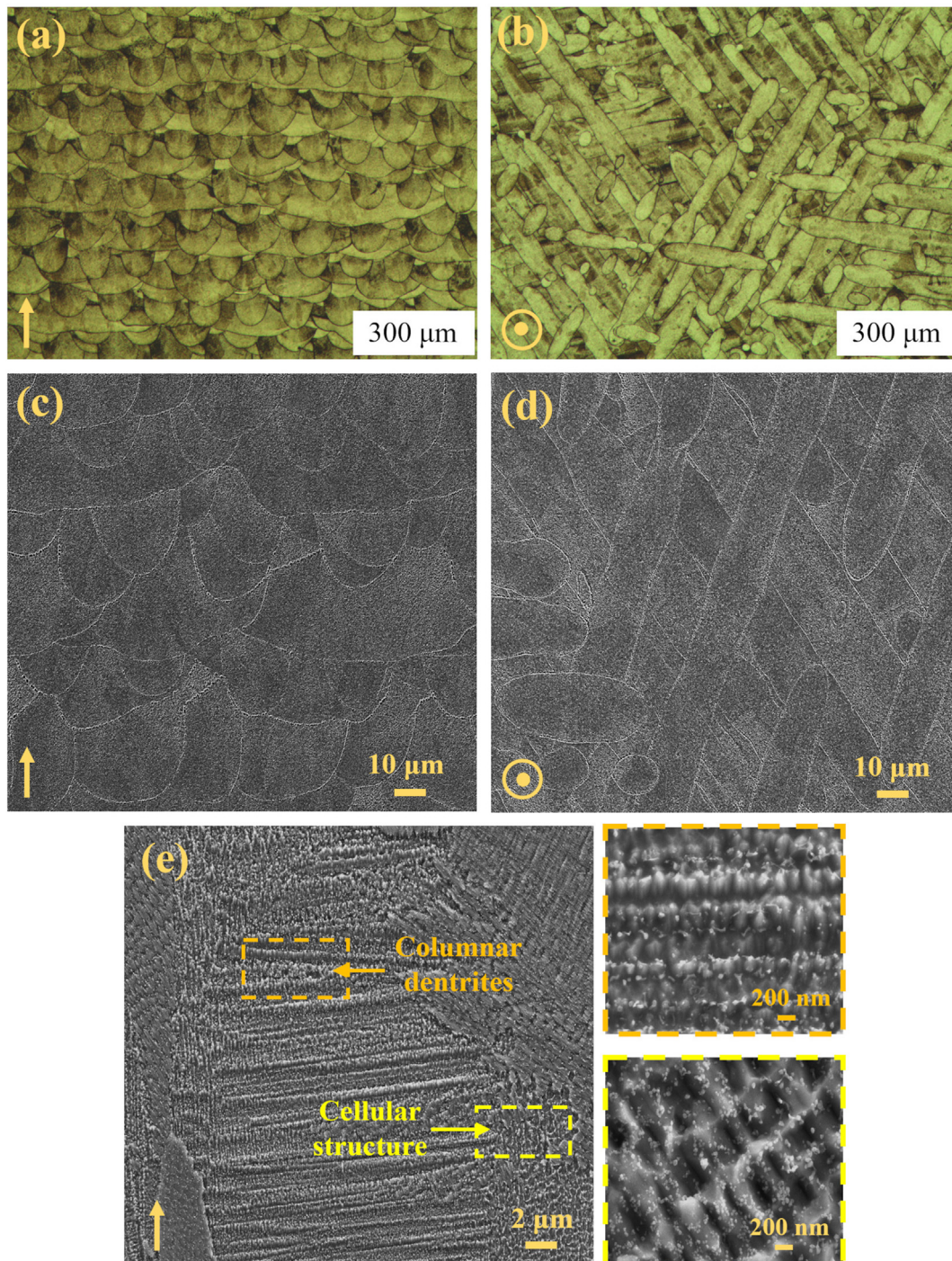
Fig. 4 − **Optical microscope and SEM images of the as-fabricated IN939 sample: (a, c) the melt pool morphology in the XZ-plane, (b, d) the laser beam scanning paths in the XY-plane (XZ- and XY- planes are shown with an arrow and a dot, respectively) and (e) the high magnification image showing the cellular and columnar structures developed within the matrix.**

intensity values of the as-fabricated sample were determined as 2.875 for IPFs and 2.989 for PFs. When we compare the solution heat-treated samples among themselves, the maximum intensity values of IPFs and PFs increased with increasing solution heat treatment temperature.

The kernel average misorientation (KAM) and grain orientation spread (GOS) maps of the as-fabricated and solution heat-treated samples were displayed in Fig. 12(a−e) and Fig. 12(f−j), respectively. KAM is examined to estimate the local misorientations, which is also related to dislocation density. In other words, a large KAM value represents a higher defect (e.g., dislocation) density. As can be seen in Fig. 12(a), the rapid solidification rate of the PBF-LB processing causes local strain inhomogeneity, accordingly formation of high
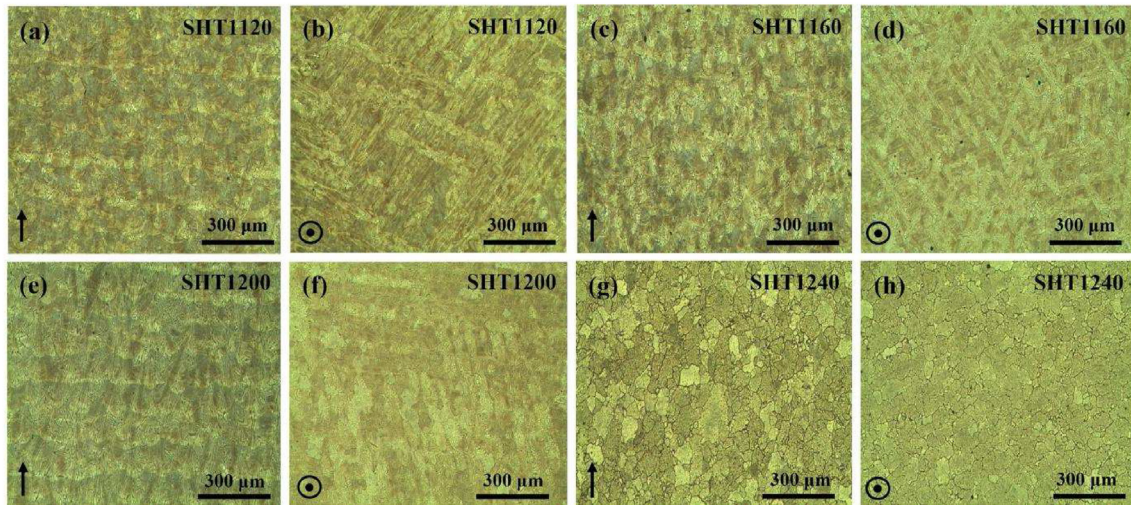
Fig. 5 — Optical microscope images of the solution heat-treated samples: (a, b) SHT1120, (c, d) SHT1160, (e, f) SHT1200 and (g, h) SHT1240 in the XZ- and XY-planes, respectively.

dislocation density in the as-fabricated sample. In the SHT1120 sample (Fig. 12(b)), there was no significant difference when compared to the as-fabricated one, possibly due to the similar microstructure present in the samples. However, the dislocation density was decreased with increasing solution heat treatment temperature, as expected (Fig. 12(c−e)).
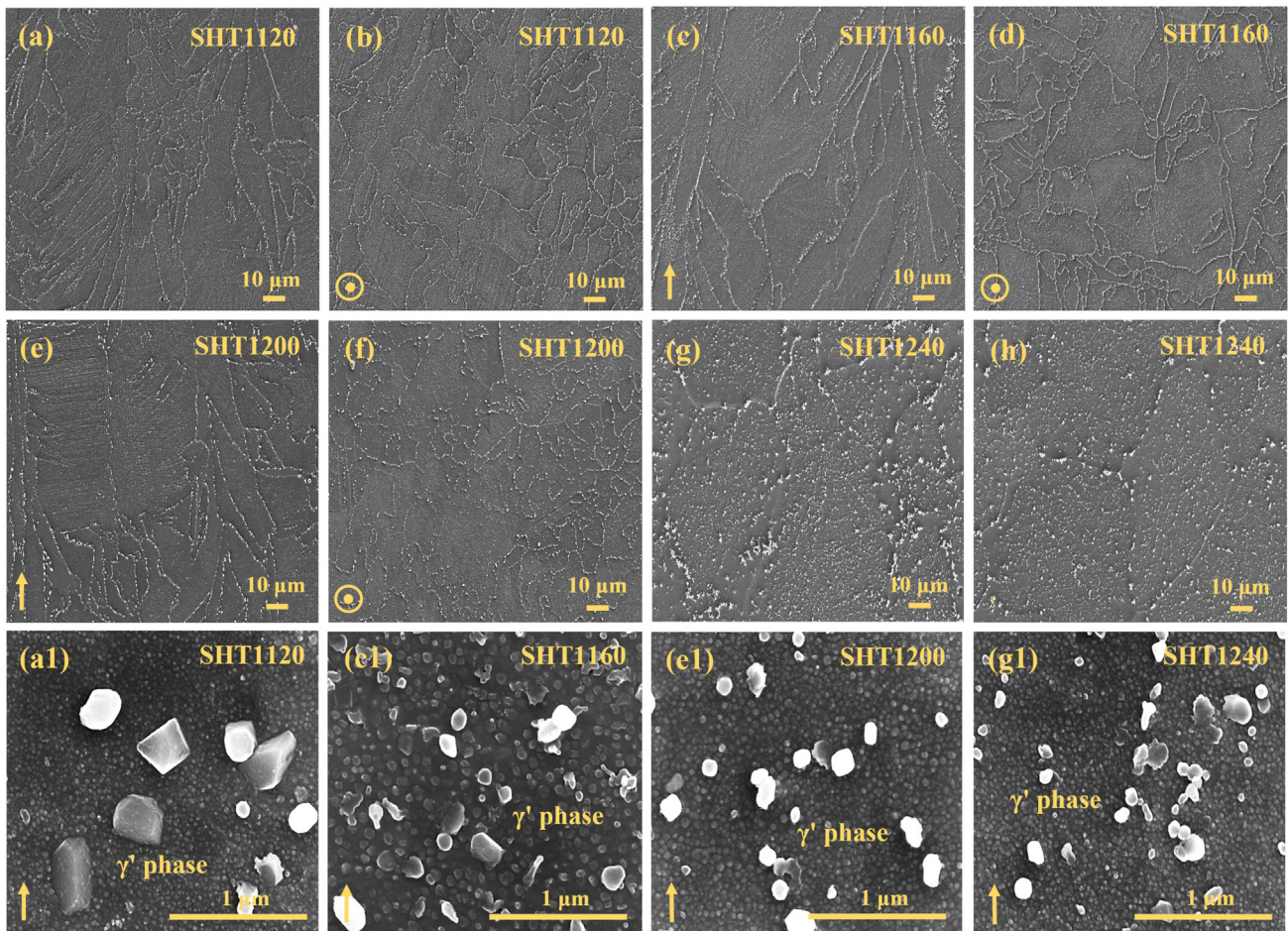

Fig. 6 — SEM images of the solution heat-treated samples: (a, b) SHT1120, (c, d) SHT1160, (e, f) SHT1200 and (g, h) SHT1240 in the XZ- and XY-planes, respectively, and (a1, c1, e1, g1) magnified images of the solution heat-treated samples, showing γ′ phases along with MC-type carbides.

Fig. 7 — SEM image of the SHT1160-treated sample showing the MC type carbides.

Grain orientation spread (GOS) maps shown in Fig. 12(f—j) represent grain based local misorientations. For GOS calculations first the average orientation of a grain is calculated. Then the misorientation between this average and the orientation of each individual measurement point within the grain is calculated. Lastly, the average of these misorientations is calculated and assigned to each point within the grain. Fully recrystallized grains have very low GOS values, whereas high defect density and deformation increases GOS. As shown in Fig. 12(h), the first recrystallized grains were observed when the samples were solution heat treated at 1160 °C. Also, increasing the solution heat treatment temperature caused an increase in the recrystallization fraction.

For better quantification, the distributions of KAM and GOS maps in the as-fabricated and solution heat-treated samples are also given in Fig. 13. The KAM distributions of both as-fabricated and solution heat-treated samples exhibited a single peak (Fig. 13(a)). The as-fabricated and SHT1120 samples had a close peak value of around 0.64 and 0.68°, respectively. Whereas the other solution heat-treated samples had lower peak values of around 0.52 for the SHT1160 and SHT1200 samples and 0.41 for the SHT1240 sample. The decrease in dislocation density after solution heat treatments caused a decrease in KAM values. It is known that the GOS distributions are highly affected by the changes in the grain structure and the characteristics of the phases formed in the structure. In our cases, the smaller grains' orientation spread is lower than those of larger grains, especially for the SHT1240 sample (as given in Fig. 13(b)). Similar to the KAM values, the GOS values of the as-fabricated and SHT1120 samples were also close to each other and were determined as 1.98 and 1.92, respectively.

However, with increasing solution heat treatment temperature, the value decreased to 1.74 for SHT1160, 1.56 for SHT1200 and 0.44 for SHT1240 due to the recrystallization of the grains.

The dislocation density in metallic materials includes geometrically necessary dislocations (GND) and statistically stored dislocations. It is reported that GNDs account for most dislocations in FCC cubic metals [22], thus GND density (Fig. 14(a)) obtained from the EBSD analyses can be used to estimate the effect of the production with PBF-LB as well as the effect of solution heat treatment on the dislocation density. The average GND density of the as-fabricated sample was determined as $36.4 \cdot 10^{12}$ m/m^3 which was close to the SHT1120 samples with an average of $35.3 \cdot 10^{12}$ m/m^3. With increasing solution heat treatment temperature, the value decreased to $28.7 \cdot 10^{12}$ m/m^3 for SHT1160, $25.9 \cdot 10^{12}$ m/m^3 for SHT1200, and $10.9 \cdot 10^{12}$ m/m^3 for SHT1240 samples, probably due to the recrystallization of the grains. Furthermore, the misorientation angle distributions are given in Fig. 14(b). The light green line represents the Mackenzie distribution for completely random oriented cubic crystals. As expected, the misorientation distribution of the as-fabricated sample exhibited the predominance of low-angle grain boundaries (<10°), implying that the grains were composed of substructure and dislocations, as also observed in the high-magnification SEM images (Fig. 4(e)). When the samples subjected to the solution heat treatment, the misorientation distribution within the grains exceeded 15° and even approached the Mackenzie distribution for the SHT1240 sample. This indicates randomization of the crystallographic texture during the heat treatment.

3.3. Microhardness measurements of the as-fabricated and solution heat-treated IN939 samples

The average Vickers microhardness values of the samples in as-fabricated and solution heat-treated conditions are tabulated in Table 5. The hardness measurements were conducted on both observation planes. As can be seen in Table 5, the hardness value of the as-fabricated sample increased with the application of solution heat treatment. As mentioned previously (Fig. 6), spherical-like γ' phase was observed for all of the solution heat treatment temperatures. The peak hardness values were observed as 531 ± 17 HV and 503 ± 14 HV for XZ- and XY-planes, respectively, when the samples were subjected to solution heat treatment at 1120 °C. On the other hand, the hardness values decreased with increasing solution heat treatment temperatures, which can be attributed to the increase in the average grain size (Fig. 11 and Table 4) and decrease in the GND density values (Fig. 14(a)). The reduction of GND density can be attributed to recrystallization phenomena, as clearly shown in the GOS maps (Fig. 12(f—j)), and

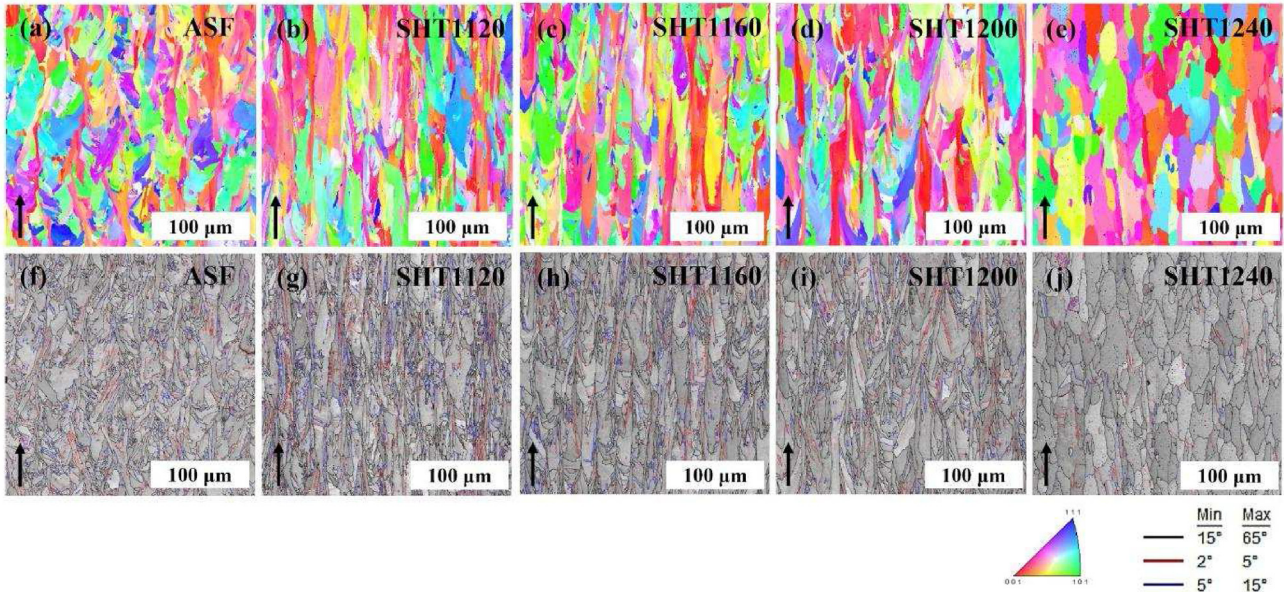| Table 3 — EDS analyses of the MC-type carbides formed in the IN939 matrix.									
Elements (wt.%)									
EDS spot	Ni	Co	Cr	Ti	Nb	W	Ta	Al	C
1	32.86	12.96	17.61	11.46	4.01	1.27	8.49	1.24	10.01
2	15.06	5.78	8.78	20.54	10.06	1.58	18.96	1.11	17.57
3	48.25	18.6	22.63	3.88	0.34	1.18	0.48	1.47	3.18

Fig. 8 – **(a–e)** IPF and **(f–j)** IQ-GBs maps of the as-fabricated and solution heat-treated IN939 samples in the XZ-plane.

this is also another reason for the reduction in the hardness values.

4. Discussion

4.1. Microstructural evolution of the as-fabricated and solution heat-treated IN939 samples

The analyzes did not reveal any significant differences in the relative densities of the IN939 samples. For both as-fabricated and solution heat-treated samples, only some lack of fusion regions and gas pores were detected; other than that, no

cracks were found in the structure, as given in Fig. 3. Such defects can occur because some of the powders that are greater than the layer thickness may lead to insufficient melting during the PBF-LB processing and result in lack-of-fusion regions in the structure. In this work, the layer thickness was set at 0.04 mm and the range of powder particle size was 17.6–52.6 μm. On the other hand, gas pores may form due to the trapping of gases dissolved in the molten metal or released from the starting powder in the molten pools [23]. It is known that the process parameters (i.e., scanning strategy, laser power and speed, hatch distance and layer thickness and etc.) of the PBF-LB method strongly influence the physical properties of the produced components [24]. Since other
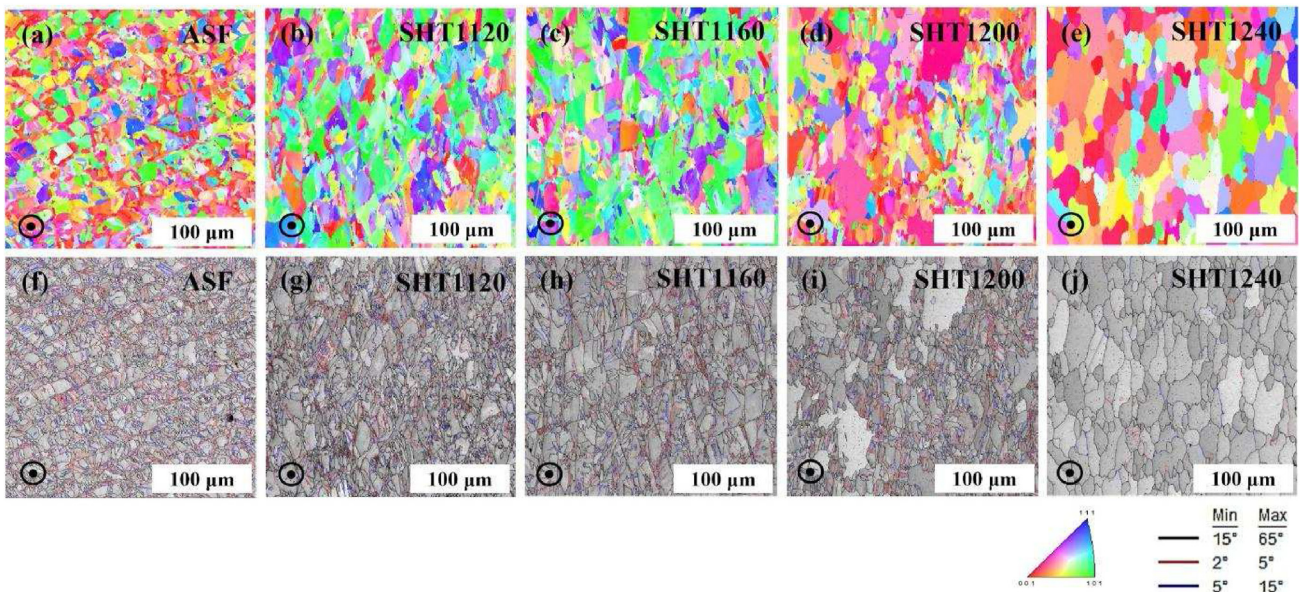

Fig. 9 – **(a–e)** IPF and **(f–j)** IQ-GBs maps of the as-fabricated and solution heat-treated IN939 samples in the XY-plane.

**Table 4 — Average grain size diameter of the as-fabricated and solution heat-treated IN939 samples.**

| Observation direction	The area-weighted average grain size diameter (μm)				
	ASF	SHT1120	SHT1160	SHT1200	SHT1240
XZ-plane	10.8 ± 1.1	16.6 ± 1.2	17.7 ± 2.3	23.5 ± 3.8	31.1 ± 5.3
XY-plane	21.3 ± 4.6	24.4 ± 3.3	25.9 ± 3.1	28.7 ± 3.5	33.8 ± 4.8

precipitation-hardenable nickel-based superalloys such as IN718 have been studied for a long time, there are many studies in the literature on process parameter optimization, heat treatment and even alloying addition for these materials. Despite the few studies on IN939, there are many shortcomings that need to be worked on. The process parameters used in our study can contribute to the studies on production optimization since micro or macro cracks were not observed in the materials. Note that the hot isostatic pressing (HIP) process is one of the effective methods used to eliminate process-induced defects in the nickel-based superalloys. Rezaei et al. [25] studied the effect of the HIP process on the as-produced and standard heat-treated IN718 alloy in terms of relative density, microstructure, and room- and high-temperature mechanical behaviors. They reported that the relative density of the as-produced sample was increased from 99.50% to 99.96% due to the elimination of the intrinsic porosities and large contour defects observed near the surfaces. They also found that the anisotropy in mechanical properties and microstructure were highly enhanced after HIP process.

The grain morphology (i.e., planar, cellular structure and columnar dendrites) of the samples fabricated with additive manufacturing methods is mainly dependent on the ratio of the thermal gradient (G) to the solidification rate (R) which is described as the G/R ratio [26,27]. It can be said that the G/R ratio for the PBF-LB processing is relatively low due to the rapid solidification rate ($(10^3-10^8$ K/s) [28]. Therefore, such columnar and cellular structures formed in the melt pool morphology and laser scanning paths detected in the XZ and XY-planes, respectively, can be developed in produced parts, as shown in Fig. 4. Further investigation revealed that the size of the columnar grains was larger than the melt pools (Fig. 8(a) and (f)), and some overlapping regions were observed, particularly in the XZ-plane (Fig. 4(a)). The occurrence of this type of morphology can be attributed to the remelting of previously solidified layers due to the thermal gradient, which

provides a strong bonding between successively deposited layers and results in better mechanical properties [29]. After the solution heat treatments, the microstructure composed of columnar elongated grains in the XZ-plane and equiaxed grains in the XY-plane were observed for the SHT1120, SHT1160 and SHT1200 samples (Figs. 8 and 9). The main difference between solution heat-treated samples is that the average grain size of the samples increased with increasing solution heat treatment temperature. On the other hand, equiaxed grains with an average size of 32 μm were observed in the SHT1240 sample for both observation directions. This grain morphology contributes to microstructural anisotropy, which is then reduced significantly when the solution heat treatment was applied at 1240 °C (Fig. 11 and Table 4).

As mentioned earlier, segregation of certain elements is one of the limitations of the PBF-LB processing which results in the formation of various brittle TCP phases such as the η (eta) phase as well as some MC and $M_{23}C_6$ type (i.e., Ti-, Ta-, Nb- and/or Cr-, W-rich, respectively) carbides. It is mostly reported that these phases negatively influence the mechanical properties of the alloys because they act as nucleation sites for crack formation [30]. However, it also should be noted that the effect of carbides on tensile properties is strongly dependent on the characteristics, including morphology, size, amount and distribution of them [31]. As given in Fig. 7 and Table 3, some irregular-shaped MC type carbides enriched with Ti, Nb and Ta elements were found at the grain boundaries and inside the grains for all conditions. The average size of the carbides was measured to be ~0.7 μm, which is smaller than that found in conventionally manufactured counterparts. The slow cooling rate of conventional manufacturing methods results in the formation of larger block-shaped carbides in the structure [27]. Moreover, the EDS results obtained from EDS spot 1 (see Fig. 7 and Table 3) indicated the concentrations of C, Ta, Ti and Nb elements in that MC carbide were considerably lower than for the MC carbide at EDS spot 2. Conversely, Ni, Cr and Co concentrations increased. In the
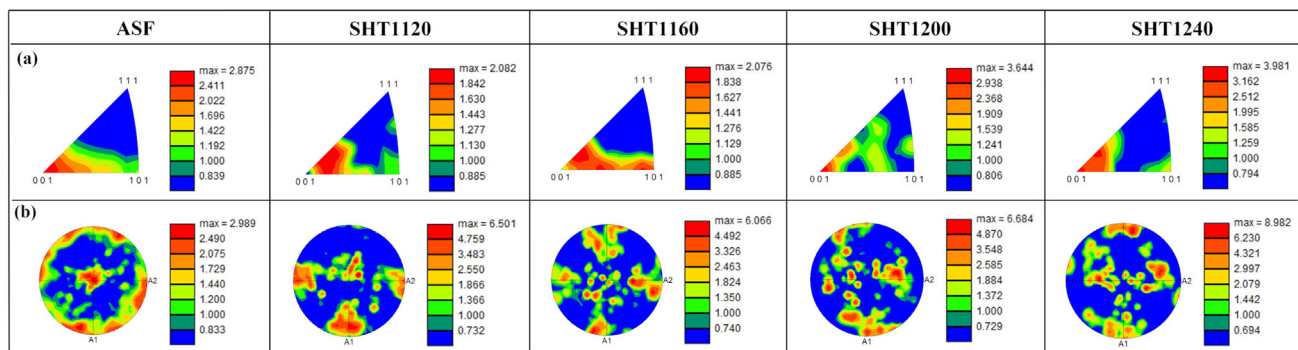
Fig. 10 — IPF and PF maps of the as-fabricated and solution heat-treated IN939 samples in the XZ-plane.
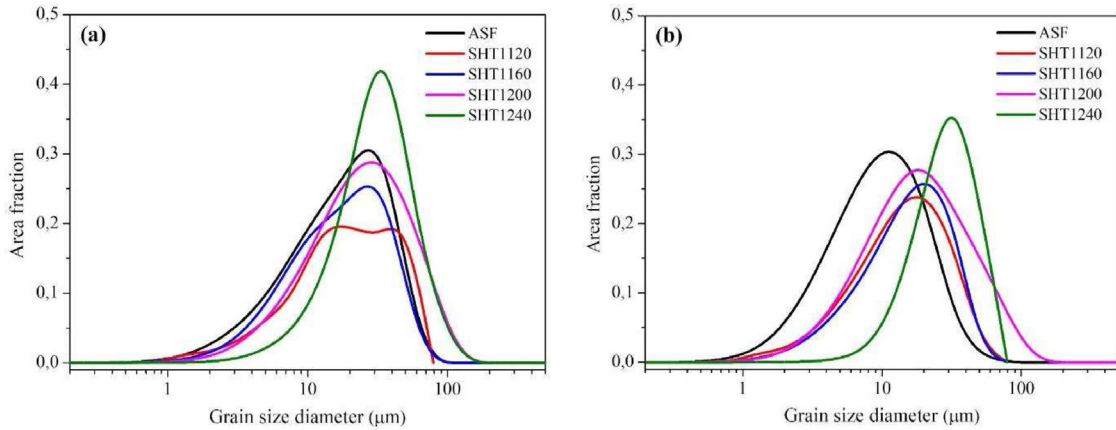
Fig. 11 – Grain size distributions of the as-fabricated and solution heat-treated IN939 samples for both observation directions: (a) in the XZ-plane, and (b) in the XY-plane.

literature, it is mentioned that there are two different transformations related to this, as given below. The first is attributed to the precipitation of the brittle η phase (Ni$_3$(Ti, Ta, Nb, Al)) and the second to the precipitation of the strengthening γ′ phase, along with formation of the M$_{23}$C$_6$ type carbide which are formed by the following reactions, respectively [32];

$$MC + \gamma \rightarrow M_{23}C_6 + \eta \qquad (2)$$

$$MC + \gamma \rightarrow M_{23}C_6 + \gamma' \qquad (3)$$

Jahangiri [33] reported that the η phase with platelet morphology is enriched with Cr, Co, Ta, Nb and Al elements. The concentration distribution of the elements is different from our studies and, no platelet-like phases were observed during the microstructural observations.

As mentioned in Section 3.3, the hardness of the as-fabricated sample increased after solution heat treatments. It is known that most of the contribution to the mechanical properties of the IN939 alloy arises from the formation of γ′ phase. As shown in the high magnification SEM images in Fig. 6(a1, c1, e1, g1), solution heat treatment led to the precipitation of spherical-like nano-sized γ′ phase within the

matrix, which is consistent with the obtained hardness results.

4.2. Texture evolution of the as-fabricated and solution heat-treated IN939 samples

The EBSD analyses were performed to address a comprehensive investigation of the effect of various solution heat treatments on the crystallographic texture, grain morphology, and recrystallization phenomena. As given in the corresponding IPFs and PFs (Fig. 10), the <001>//BD texture was dominant for all samples. The solution heat treatments did not cause a significant change in the texture of the samples produced, but still affected their maximum intensity values. These values were highest for SHT1240 samples (i.e., 3.981 for IPF and 8.982 for PF) most likely due to recrystallization and subsequent grain growth mechanism. IQ & GBs maps of the samples showed that the as-fabricated and SHT1120 samples contained high amounts of low-angle grain boundaries (LAGBs), indicated by the red and blue lines. As seen in the figures of SHT1160 and SHT1200 samples, LAGB density decreased with increasing solution heat treatment temperature. The
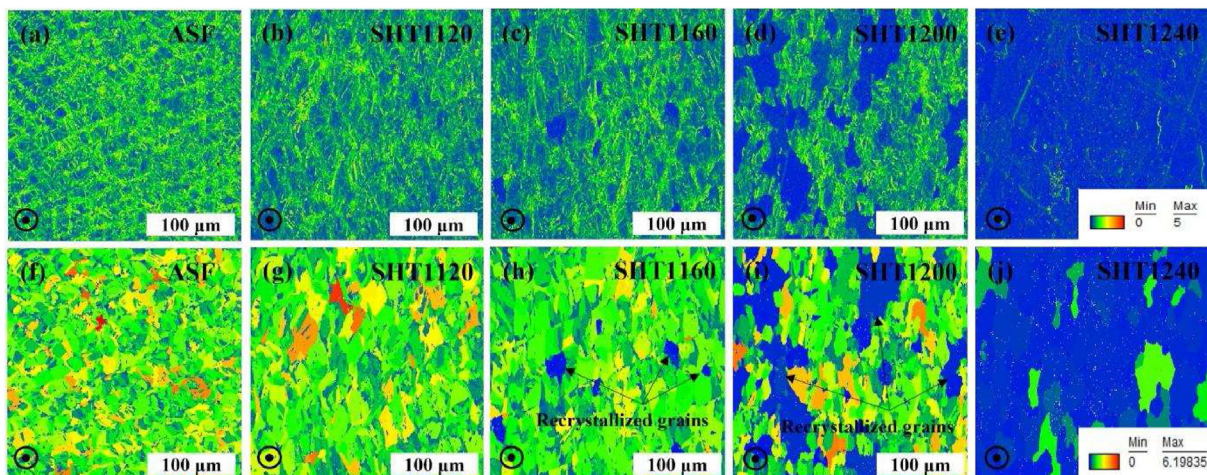
Fig. 12 – (a–e) KAM and (f–j) GOS maps of the as-fabricated and solution heat-treated IN939 samples in the XY-plane.
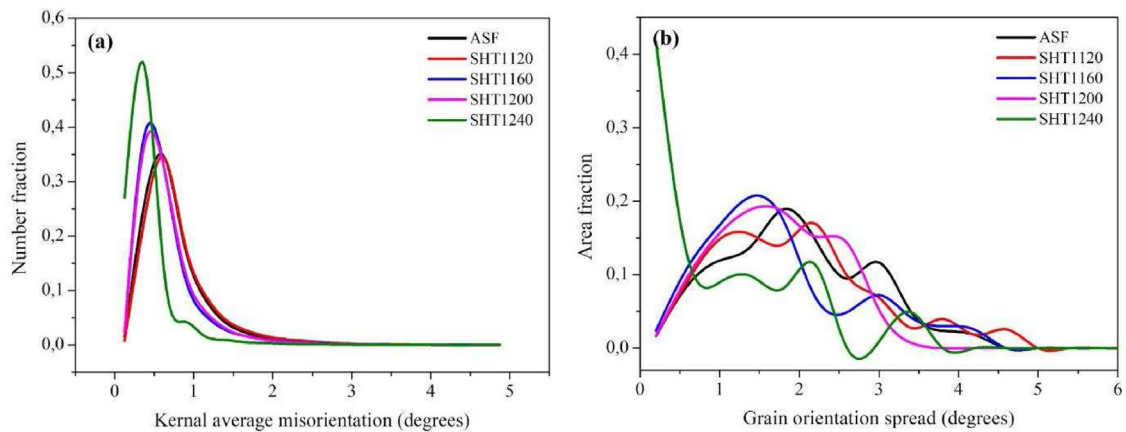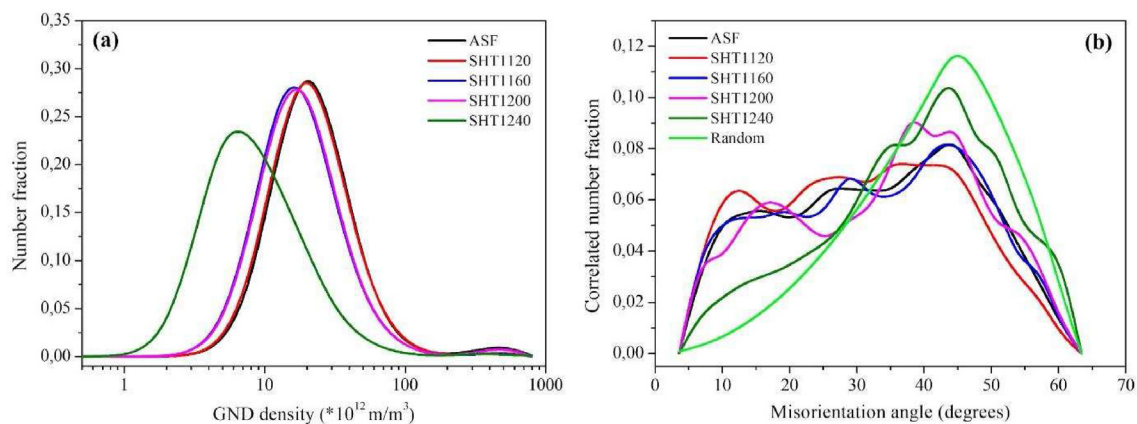
Fig. 13 − (a) KAM and (b) GOS distributions of the as-fabricated and solution heat-treated IN939 samples in the XY-plane.

misorientation distribution of the samples also indicated that most of the grain boundaries are LAGBs, as given in Fig. 14(b). On the other hand, these boundaries changed into high-angle grain boundaries (HAGBs) and approached the Mackenzie distribution for the SHT1240 sample, which is attributed to the randomization of texture due to recrystallization phenomenon.

It is well known that the high-temperature gradient and rapid solidification rate of the PBF-LB processing cause high defect density along with the high residual stress in the fabricated parts. According to the results obtained from KAM (Fig. 12(a−e)) and GND (Fig. 14(a)) analyses, it was observed that the as-fabricated sample had high dislocation densities, especially along grain boundaries rather than grain interiors. The dislocation density of the SHT1120 sample was close to its as-fabricated counterpart. The GND value decreased by 18.7%, 26.8% and 69.1% for the SHT1160, SHT1200 and SHT1240 samples, respectively. Moreover, the reduction in the KAM values (Fig. 13(a)) was calculated as approximately 23.4% for the SHT1160 and SHT1200 samples and 49.2% for the SHT1240 sample. It can be revealed that a significant decrease in both dislocation density and residual stress were observed with increasing solution heat treatment temperature.

GOS is also used to distinguish recrystallized grains from others. Grains with a GOS value less than 1.5 represent recrystallized ones [34]. As seen in the GOS maps and distributions (and Fig. 12(f−j) and Fig. 13(b)), the GOS values of the as-fabricated and SHT1120 sample were higher and GOS values decreased with increasing temperature of the solution heat treatment. Fig. 15 shows the recrystallization fractions of the as-fabricated and solution heat-treated samples. Here, a threshold GOS value of 1.8° was selected to distinguish recrystallized grains. The first recrystallized grains, as indicated in Fig. 12(h), began to appear when the samples were subjected to the solution heat treatment at 1160 °C and the GOS value decreased by 10.3%. The fraction of the recrystallized grains increased from 0.55 (this value was calculated for the as-fabricated sample) to 0.56 for SHT1120, 0.66 for SHT1160 and 0.68 for SHT1200 samples as the solution heat treatment temperature increased with decreasing the GOS value. Moreover, most of the grains were recrystallized for the SHT1240 sample, as its recrystallization fraction was calculated 0.97. The recrystallization starts from high defect density regions, such as overlapping melt pools and cross-over points of laser-beam scanning paths (hatch pattern). Those regions exhibit higher local misorientations and higher GND

Fig. 14 − (a) GND and (b) misorientation angle distributions of the as-fabricated and solution heat-treated IN939 samples in the XY-plane.

Observation direction	Hardness (HV1)				
	ASF	SHT1120	SHT1160	SHT1200	SHT1240
XZ-plane	358 ± 12	531 ± 17	446 ± 19	463 ± 43	448 ± 45
XY-plane	380 ± 10	503 ± 14	435 ± 24	466 ± 27	445 ± 21

Table 5 — Average Vickers microhardness values of the as-fabricated and solution heat-treated IN939 samples.

density than the rest of the sample. The local misorientations and GND density decrease with increasing solution heat treatment temperature. Those findings are in agreement with our previous study on recrystallization kinetics and grain growth in PBF-LB produced IN718 [35]. IN718 involved twinning-assisted recrystallization mechanism and exhibited significant grain growth over 1150 °C. For IN939 the distribution of defects (i.e., dislocations) coming from the as-fabricated structure, and the size and distribution of TCP phases and MC type carbides determine the recrystallization kinetics of IN939. It was also found that the carbides and precipitates limited the grain growth of IN939, compared to IN718.

5. Conclusions

The effect of solution heat treatment on the microstructure, grain morphology and crystallographic texture of the IN939 fabricated by the PBF-LB method were systematically investigated. Based on the results of this study, the main findings can be summarized as follows.

1 For solution heat treatment of 1200 °C, the arc-shaped morphologies seen in the as-fabricated samples disappeared and turned into a mixture of columnar and equiaxed grains in the XZ and XY-planes, respectively. When the samples were solution heat-treated at 1240 °C, microstructural anisotropy was eliminated by forming equiaxed grains with an average size of 32 μm.
2 Texture analyses showed that both as-fabricated and solution heat-treated samples had a preferential <001>//BD
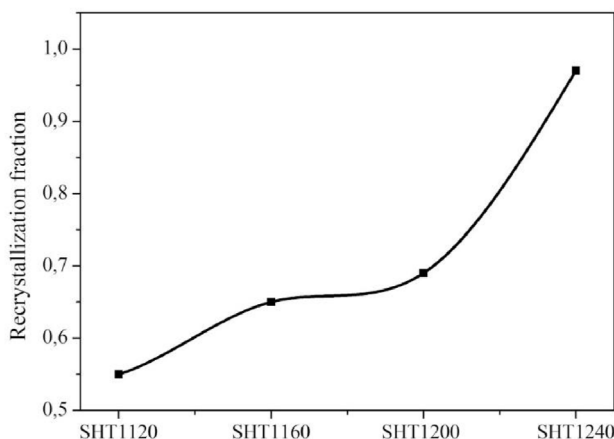
texture. The intensity values increased with increasing solution heat treatment temperature.
3 The high amount of LAGBs and GNDs density formed in the as-fabricated sample due to the high-temperature gradient and rapid solidification rate of the PBF-LB processing decreased after solution heat treatment. Moreover, their fractions decreased as the solution heat treatment temperature increased.
4 As shown in the KAM and GOS maps and distributions, the first recrystallized grains began to appear when the samples were subjected to the solution heat treatment at 1160 °C and the fraction of the recrystallized grains increased with increasing solution heat treatment temperature. Here the size and distribution of TCP phases and MC type carbides determine the recrystallization kinetics, and they also limit the grain growth.
5 High magnification SEM images showed that a large amount of spherical-like nano-sized the γ' phase formed within the matrix after all solution heat treatment conditions, which caused to increase in the hardness values.

Credit authorship contribution statement

Merve Nur Doğu: Conceptualization, Methodology, Investigation, Data curation, Writing - review & editing, Visualization, Project administration. **Seren Özer:** Conceptualization, Methodology, Investigation, Data curation, Writing - original draft, Writing - review & editing, Visualization, Project administration. **Mustafa Alp Yalçın:** Investigation. **Kemal Davut:** Conceptualization, Methodology, Writing - Review & Editing. **Güney Mert Bilgin:** Methodology. **Muhannad Ahmed Obeidi:** Investigation. **Håkan Brodin:** Writing — review & editing. **Hengfeng Gu:** Writing — review & editing, Funding acquisition. **Dermot Brabazon:** Conceptualization, Validation, Resources, Writing - review & editing, Supervision, Project administration, Funding acquisition.

Data statement

The raw/processed data required to reproduce these findings cannot be shared at this time as the data also forms part of an ongoing study.

Fig. 15 — Recrystallization fractions of the as-fabricated and solution heat-treated samples.

Declaration of competing interest

The authors declare that they have no known competing financial interests or personal relationships that could have appeared to influence the work reported in this paper.

Acknowledgments

REFERENCES

[1] Marchese G, Parizia S, Saboori A, Manfredi D, Lombardi M, Fino P, et al. The influence of the process parameters on the densification and microstructure development of laser powder bed fused Inconel 939. Metals 2020;10:882. https://doi.org/10.3390/met10070882.

[2] Banoth S, Li CW, Hiratsuka Y, Kakehi K. The Effect of recrystallization on creep properties of alloy IN939 fabricated by selective laser melting process. Metals 2020;10:1016. https://doi.org/10.3390/met10081016.

[3] Huang W, Yang J, Yang H, Jing G, Wang Z, Zeng X. Heat treatment of Inconel 718 produced by selective laser melting: microstructure and mechanical properties. Mater Sci Eng, A 2019;750:98–107. https://doi.org/10.1016/j.msea.2019.02.046.

[4] Bean GE, Witkin DB, Mclouth TD, Patel DN, Zaldivar RJ. Effect of laser focus shift on surface quality and density of Inconel 718 parts produced via selective laser melting. Addit Manuf 2018;22:207–15. https://doi.org/10.1016/j.addma.2018.04.024.

[5] Komarasamy M, Shukla S, Williams S, Kandasamy K, Kelly S, Mishra RS. Microstructure, fatigue, and impact toughness properties of additively manufactured nickel alloy 718. Addit Manuf 2019;28:661–75. https://doi.org/10.1016/j.addma.2019.06.009.

[6] Chlebus E, Gruber K, Ku B, Kurzac J, Kurzynowski T. Effect of heat treatment on the microstructure and mechanical properties of Inconel 718 processed by selective laser melting. Mater Sci Eng, A 2015;639:647–55. https://doi.org/10.1016/j.msea.2015.05.035.

[7] Li X, Shi JJ, Wang CH, Cao GH, Russell AM, Zhou ZJ, et al. Effect of heat treatment on microstructure evolution of Inconel 718 alloy fabricated by selective laser melting. J Alloys Compd 2018;764:639–49. https://doi.org/10.1016/j.jallcom.2018.06.112.

[8] Liu P, Hu J, Sun S, Feng K, Zhang Y, Cao M. Microstructural evolution and phase transformation of Inconel 718 alloys fabricated by selective laser melting under different heat treatment. J Manuf Process 2019;39:226–32. https://doi.org/10.1016/j.jmapro.2019.02.029.

[9] Shaikh AS. Development of a γ′ precipitation hardening Ni-base superalloy for additive manufacturing. Thesis 2018. https://doi.org/10.13140/RG.2.2.11472.81921.

[10] Ni M, Liu S, Chen C, Li R, Zhang X, Zhou K. Effect of heat treatment on the microstructural evolution of a precipitation-hardened superalloy produced by selective laser melting. Mater Sci Eng, A 2019;748:275–85. https://doi.org/10.1016/j.msea.2019.01.109.

[11] Ozer S, Bilgin GM, Davut K, Esen Z, Dericioglu AF. Effect of post fabrication aging treatment on the microstructure, crystallographic texture and elevated temperature mechanical properties of IN718 alloy fabricated by selective laser melting. J Mater Process Technol 2022;306:117622. https://doi.org/10.1016/j.jmatprotec.2022.117622.

[12] Haines MP, Rielli VV, Primig S, Haghdadi N. Powder bed fusion additive manufacturing of Ni-based superalloys: a review of the main microstructural constituents and characterization techniques. J Mater Sci 2022;57:14135–87. https://doi.org/10.1007/s10853-022-07501-4.

[13] Jahangiri MR, Arabi H, Boutorabi SMA. Development of wrought precipitation strengthened IN939 superalloy. Mater Sci Technol 2012;28. https://doi.org/10.1179/1743284712Y.0000000073.

[14] Kanagarajah P, Brenne F, Niendorf T, Maier HJ. Inconel 939 processed by selective laser melting: effect of microstructure and temperature on the mechanical properties under static and cyclic loading. Mater Sci Eng, A 2013;588:188–95. https://doi.org/10.1016/j.msea.2013.09.025.

[15] Philpott W, Jepson MAE, Thomson RC. Comparison of the effects of a conventional heat treatment between cast and selective laser melted IN939 alloy. Adv. Mater. Technol. Foss. Power Plants - Proc. from 8th Int. Conf. 2016:735–46.

[16] Shaji Karapuzha A, Fraser D, Zhu Y, Wu X, Huang A. Effect of solution heat treatment and hot isostatic pressing on the microstructure and mechanical properties of Hastelloy X manufactured by electron beam powder bed fusion. J Mater Sci Technol 2022;98:99–117. https://doi.org/10.1016/j.jmst.2021.04.059.

[17] Bunge HJ. Introduction, texture analysis in materials science. 1982. https://doi.org/10.1016/b978-0-408-10642-9.50006-4.

[18] ASTM B962: Standard test methods for density of compacted or sintered powder metallurgy (PM) products using Archimedes' Principle. ASTM International.

[19] Li J, Zhao Z, Bai P, Qu H, Liu B, Li L, Wu L, Guan R, Liu H, Guo Z. Microstructural evolution and mechanical properties of IN718 alloy fabricated by selective laser melting following different heat treatments. J Alloys Compd 2019;772:861–70. https://doi.org/10.1016/j.jallcom.2018.09.200.

[20] Wang Z, Guan K, Gao M, Li X, Chen X, Zeng X. The microstructure and mechanical properties of deposited-IN718 by selective laser melting. J Alloys Compd 2012;513:518–23. https://doi.org/10.1016/j.jallcom.2011.10.107.

[21] Popovich V, Borisov EV, Popovich AA, Sufiiaro VS, Masaylo DV, Alzina L. Impact of heat treatment on mechanical behaviour of Inconel 718 with tailored microstructure processed by selective laser melting. Mater Des 2017;131:12–22. https://doi.org/10.1016/j.matdes.2017.05.065.

[22] Zhang S, Lin X, Wang L, Yu X, Hu Y, Yang H, Lei L, Huang W. Strengthening mechanisms in selective laser-melted Inconel 718 superalloy. Mater Sci Eng, A 2021;812:141145. https://doi.org/10.1016/j.msea.2021.141145.

[23] Zhang X, Xu H, Li Z, Dong A, Du D, Lei L, et al. Effect of the scanning strategy on microstructure and mechanical anisotropy of Hastelloy X superalloy produced by Laser Powder Bed Fusion. Mater Char 2021;173:110951. https://doi.org/10.1016/j.matchar.2021.110951.

[24] Zhang B, Li Y, Bai Q. Defect formation mechanisms in selective laser melting: a review. Chinese J. Mech. Eng. (English Ed. 2017;30:515–27. https://doi.org/10.1007/s10033-017-0121-5.

[25] Rezaei A, Kermanpur A, Rezaeian A, Badrossamay M, Foroozmehr E, Sadeghi F, et al. Contribution of hot isostatic pressing on densification, microstructure evolution, and mechanical anisotropy of additively manufactured IN718 Ni-based superalloy. Mater Sci Eng, A 2021;823:141721. https://doi.org/10.1016/j.msea.2021.141721.

[26] Dogu MN, McCarthy E, McCann R, Mahato V, Caputo A, Bambach M, Ahad IU, Brabazon D. Digitisation of metal AM for part microstructure and property control. Int J Material Form 2022;15. https://doi.org/10.1007/s12289-022-01686-4.

[27] Jena A, Atabay SE, Brochu M. Microstructure and mechanical properties of crack-free Inconel 738 fabricated by laser powder bed fusion. Mater Sci Eng, A 2022;850:143524. https://doi.org/10.1016/j.msea.2022.143524.

[28] Gallmeyer TG, Moorthy S, Kappes BB, Mills MJ, Amin-Ahmadi B, Stebner AP. Knowledge of process-structure-property relationships to engineer better heat treatments for laser powder bed fusion additive manufactured Inconel 718. Addit Manuf 2020;31:100977. https://doi.org/10.1016/j.addma.2019.100977.

[29] Malý M, Nopová K, Klakurková L, Adam O, Pantělejev L, Koutný D. Effect of preheating on the residual stress and material properties of Inconel 939 processed by laser powder bed fusion. Materials 2022;15:6360. https://doi.org/10.3390/ma15186360.

[30] Cao X, Zhang YN, Wanjara P, Medraj M. Tensile properties of laser additive manufactured Inconel 718 using filler wire. J Mater Res 2014;29:2006—20. https://doi.org/10.1557/jmr.2014.199.

[31] Zhao Y, Guan K, Yang Z, Hu Z, Qian Z, Wang H, Ma Z. The effect of subsequent heat treatment on the evolution behavior of second phase particles and mechanical properties of the Inconel 718 superalloy manufactured by selective laser melting. Mater Sci Eng, A 2020;794:139931. https://doi.org/10.1016/j.msea.2020.139931.

[32] Jahangiri MR, Abedini M. Effect of long time service exposure on microstructure and mechanical properties of gas turbine vanes made of IN939 alloy. Mater Des 2014;64:588—600. https://doi.org/10.1016/j.matdes.2014.08.035.

[33] Jahangiri MR, Arabi H, Boutorabi SMA. Investigation on the dissolution of η phase in a cast Ni-based superalloy. Int J Miner Metall Mater 2013;20:42—8. https://doi.org/10.1007/s12613-013-0691-x.

[34] Xu J, Ding Y, Gao Y, Wang H, Hu Y, Zhang D. Grain refinement and crack inhibition of hard-to-weld Inconel 738 alloy by altering the scanning strategy during selective laser melting. Mater Des 2021;209:109940. https://doi.org/10.1016/j.matdes.2021.109940.

[35] Doğu MD, Davut K, Obeidi MA, Yalçın MA, Gu H, Low TSE, Ginn J, Brabazon D. Recrystallization and grain growth kinetics of IN718 manufactured by laser powder bed fusion. J Mater Res Technol 2022;19:4242—57. https://doi.org/10.1016/j.jmrt.2022.06.157.